4. WAVE SYSTEMS IN THE MEDITERRANEAN SEA

4.1. Introduction

The wave hindcast developed for the Pacific Coast of Central America provides a sound benchmark of integral parameters, which can be used for a variety of engineering projects. Indeed, as shown in the previous Chapters, significant wave heights and mean and peak periods can summarize the potential wave energy to be extracted at a given site [Robertson et al., 2016], and provide information about extreme states that lay the foundations for the design of offshore and coastal infrastructures [Wu et al., 2015].

However, the integral parameters do not capture the variability of different wave systems during multimodal sea states, i.e., those seas encompassing both wind seas locally generated and swell waves that already left their area of generation [Munk, 1951]. This information may be relevant especially in case multiple systems propagate along different directions; indeed, such condition could give origin to the combination, or permutations of these wave systems. A special case of permutations takes place which is corresponds to the crossing seas, that are particularly dangerous for the safety of navigation [Xu et al., 2020, Mayer et al., 2018, Leone, 2017].

Crossing seas occur when multiple wave systems propagating from different directions co-exist; commonly, when a wave system still in the generation and growing phase crosses one or multiple swells, i.e., long waves that have already left their generation area [Semedo et al., 2011].

On this note, this chapter presents a collaborative research wherein a novel methodology for the detection of relevant directional wave patterns has been developed. The method is based on the Otsu method for picture segmentation as detailed in section 4.2.1. A further analysis on the wave systems occurrence, including the wave systems in crossing seas, is described in section 4.2.3. further on in the text. This procedure was applied at multiple hindcast nodes in the Mediterranean Sea (see Figure 4.1), and the resulting systems are available through a WebGIS developed for this study.

4.2. Wave systems for multimodal sea states: Methodology

The wave hindcast data employed in for the wave systems detection has been developed by the Department of Civil, Chemical and Environmental Engineering of the University of Genoa [Mentaschi et al., 2013]. Information over the Mediterranean Sea basin under a spatial resolution of 0.1273 $°\times$ 0.09 $°$ and a time span 1979 to 2020 at a hourly resolution.

This study assess the wave energy density spectra at the studied span, however spectral parameters have been required from the integration of such spectra. The integral parameters are the H_{m0}, mean spectral wave period (T_m), mean wave direction (θ_m), and the peak parameters

T_p and θ_p, and they are extracted for both the whole spectrum and for three spectral partitions referring to wind waves and to primary and secondary swells.

The wave systems detection has been carried out for all the nodes belonging to the Mediterranean Sea domain. For the sake of simplicity, the results obtained for a node, numbered 6858, whose longitude is 11.2900°, and latitude 38.8200°, is shown in the Figure 4.1.
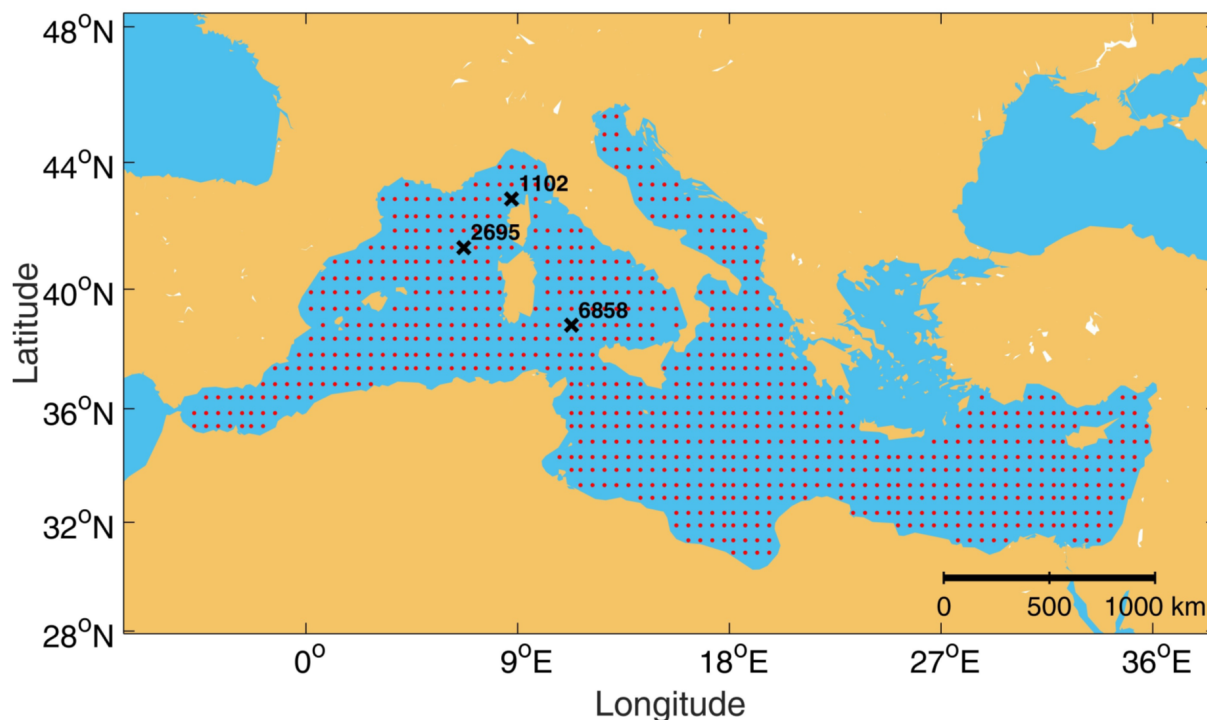

Figure 4.1: Studied locations along the Mediterranean Sea. Red points highlight the hindcast nodes employed for the research. Black crosses denote the nodes representing the samples described in this section.

The relevance of employing this pixels' segmentation method lies in the fact that sometimes when evaluating certain parameters, such as the mean wave direction of the peak wave frequency, it does not necessarily represent the real energy distribution not only in direction but also in frequencies. The Figure 4.2 shows an energy density spectrum recorded in the Ligurian Sea; there are methodologies that would indicate that the direction associated with the peak frequency would be close to 180°, or South, when in fact there is a evident distinction of the wave energy density provenance from South-west (SW) and SE.

The section 4.2.1. describes the general pixel segmentation methodology proposed by Otsu [1979].

4.2.1. Image segmentation: Otsu thresholding method

The image segmentation method corresponds to a non-parametric and unsupervised method that allows separate the pixels which composes the image into two pixels classes in function of
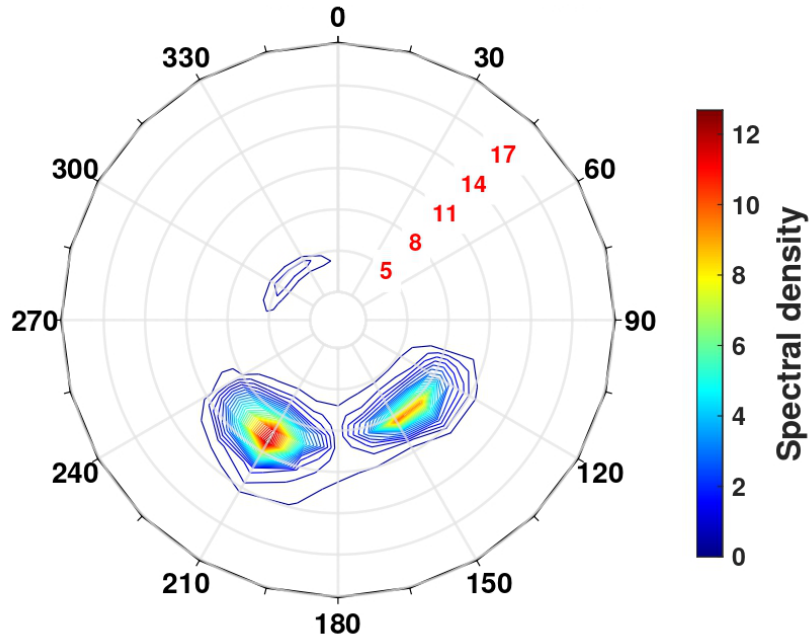
Figure 4.2: Exemplification of wave energy density spectrum and its wave systems at longitude 8.743° and latitude 43.860°.

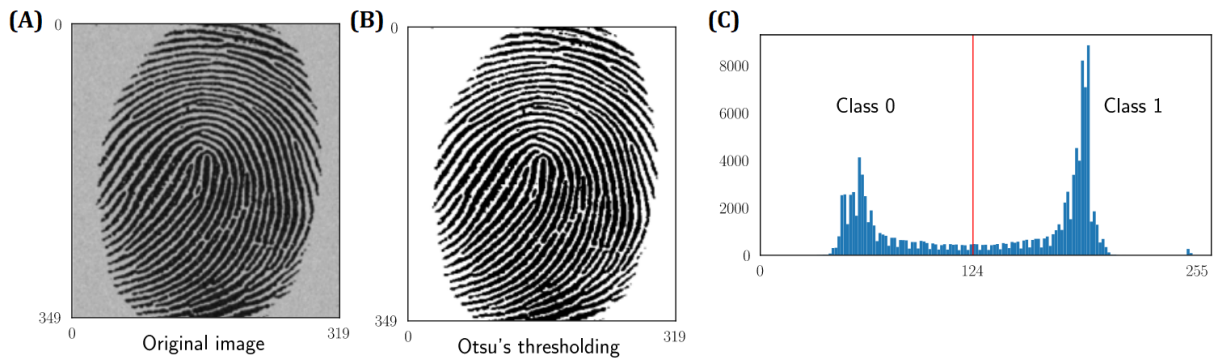the pixel intensities (also called level), as exemplified in Figure 4.3.

Figure 4.3: Otsu thresholding method: chart (A) shows the grayscale image, chart (B) the segmented image (white and black) after applied the Otsu algorithm, and chart (C) the groups separation of the histogram of pixels intensities. Source:Mazet [2023], edited by the author.

The fingerprint image in Figure 4.3(A) is composed by N number of pixels, wherein the number at the i level is denoted by n_i, and fulfilling the following conditions through L levels:

$$p_i = \frac{n_i}{N} \ , \ p >= 0 \ , \ \sum_{i=1}^{L} p_i = 1 \tag{4.1}$$

Two classes of pixels C_0 and C_1 are postulated which are sufficiently differentiated, e.g. background and objects, or white and black colours, which leads to the image in Figure 4.3(B).

To reach this, both classes are split by a threshold at level k, wherein C_0 contains the pixel level [1,2,..., k], whilst C_0 denotes with pixels [k+1, k+2, ..., L].

This methodology relies on finding the solution by means of an iterative process of the greatest dissimilarity or dichotomy of both classes, respecting the similarity between the levels of each class. For this, it is required to estimate the variances within classes and between both classes, which initially depend on the probability of occurrence (ω) of classes 1 and 2:

$$\omega_0 = \mathbf{Pr}(C_0) = \sum_{i=1}^{k} p_i = \omega(k) \,, \tag{4.2}$$

where p_i is the ratio of the number of pixels at every level over the total number of the image pixels. In the case of the second class:

$$\omega_1 = \mathbf{Pr}(C_1) = \sum_{i=k+1}^{L} p_i = 1 - \omega(k) \tag{4.3}$$

Likewise, the class mean levels (μ) are required in the estimation of the classes variance. The first class mean level is estimated by:

$$\mu_0 = \sum_{i=1}^{k} \mathbf{Pr}(i|C_0) = \sum_{i=1}^{k} \frac{i \, p_i}{\omega_0} = \frac{\mu(k)}{\omega(k)}, \tag{4.4}$$

while the second class mean level corresponds to:

$$\mu_1 = \sum_{i=1}^{k} \mathbf{Pr}(i|C_1) = \sum_{i=1}^{k} \frac{i \, p_i}{\omega_1} = \frac{\mu_T(k) - \mu(k)}{1 - \omega(k)}, \tag{4.5}$$

where:

$$\omega(k) = \sum_{i=1}^{k} p_i \,,$$
$$\mu(k) = \sum_{i=1}^{k} i \, p_i \tag{4.6}$$

Then, the total mean level of the original image corresponds to:

$$\mu_T = \mu(L) = \sum_{i=1}^{L} i \, p_i \tag{4.7}$$

Thus, it is worth noting that validity of the equation (4.8):

$$\omega_0 \mu_0 + \omega_1 \mu_1 = \mu_T \,, \; \omega_0 + \omega_1 = 1 \tag{4.8}$$

The class variances (σ^2) are calculated as follows:

$$\sigma_0^2 = \sum_{i=1}^{k} (i - \mu_0)^2 \, \mathbf{Pr}(i|C_0) = \sum_{i=1}^{k} (i - \mu_0)^2 \frac{p_i}{\omega_0} \tag{4.9}$$

where **Pr** corresponds to the probability of i given the condition C_0, and:

$$\sigma_1^2 = \sum_{i=1}^{k}(i - \mu_1)^2 \, \mathbf{Pr}(i|C_1) = \sum_{i=1}^{k}(i - \mu_1)^2 \frac{p_i}{\omega_1} \,, \tag{4.10}$$

A series of discriminant criterion measures are considered in order to evaluated the goodness of the thresholding, such measures are λ, κ, and η:

$$\lambda = \frac{\sigma_B^2}{\sigma_W^2}$$
$$\kappa = \frac{\sigma_T^2}{\sigma_W^2} \tag{4.11}$$
$$\eta = \frac{\sigma_B^2}{\sigma_T^2}$$

where:

$$\sigma_W^2 = \omega_0 \, \sigma_0^2 + \omega_1 \, \sigma_1^2, \tag{4.12}$$

$$\sigma_B^2 = \omega_0(\mu_0 - \mu_T)^2 + \omega_1(\mu_1 - \mu_T)^2, \tag{4.13}$$

and as indicated in equation (4.8), the between-classes variance is given by:

$$\sigma_T^2 = \sum_{i=1}^{L}(i - \mu_T)^2 \, p_i \tag{4.14}$$

Furthermore, the discriminant criteria lead to maximize the terms λ, κ and η, by adjusting the k, given that equation (4.14) is k-depending. On other words, the optimal threshold is obtained by solving the equation (4.15). Such optimal threshold corresponds to the red line at the chart (C) in Figure 4.3.

$$\sigma_B^2(k) = \frac{[\mu_T \, \omega(k) - \mu(k)]^2}{\omega(k) \, [1 - \omega(k)]}, \tag{4.15}$$

restricted by the range $0 < \omega(k) < 1$.

The Otsu thresholding method presents some shortcomings as the presence of noise in digital images causing random fluctuations in pixel intensity, obscuring the underlying structure of the image and affecting the accuracy of thresholding. Gaussian noise, for instance, can introduce variability in pixel values that may lead to errors in the classification during thresholding procedure [Kittler and Illingworth, 1986].

This limitation is particularly pronounced in low-contrast images or those with uneven illumination, where noise can overwhelm the signal of interest. Nonetheless, for the purposes of the wave system analysis, where there is a marked difference between the pixel intensities involved in the evaluated wave partitions, this does not represent a drawback.

Then, Otsu thresholding method described previously was herein applied to images which show the ocurrence probability of integral parameters belonging to different spectral partitions at each node, as documented in section 4.2.2.

4.2.2. Wave systems detection

The first step for the automatic detection of directional wave systems implies to build an image summarizing the variability of the local wave climate at a given hindcast node. In order to consider the most critical sea states, it is only retain data associated to a total significant wave height H_S (i.e. summed over the partitions) higher than 1 m; note that this approach slightly differs by that of Portilla-Yandún [2018], who set a common threshold for all systems at a location in the Atlantic Ocean, rather than looking at their sum. However, by using such an approach it would neglect too many data in the Mediterranean Sea, which is indeed characterized by a milder wave climate.

At a second time, it is pool together all T_m and θ_m data of the three spectral partitions that meet the condition above, and it is group the resulting dataset in 2D-bins of given width to construct a bi-variate frequency matrix. T_m is used since this parameter is commonly used to distinguish between different types of waves [Munk, 1951]. The frequency matrix is next smoothed through a 2D-Gaussian filter and processed based on the Otsu [1979] method for picture segmentation (described in section 4.2.1.).

In this case, the bins of the (T_m, θ_m) matrix can be thought of as the pixels of an image whose colors depend on the respective data frequency. Therefore, all bins can be assigned to the foreground through the Otsu [1979] algorithm, and next split between different clusters, i.e., the wave systems, based on their contiguity in the (T_m, θ_m) space. Finally, centroids of each cluster are computed based on the pixels position in the (T_m, θ_m) space; this way, each system centroid is associated to a frequent (T_m, θ_m) pair, identifying in turn the relevant fetches from which waves are originated at the study site.

The followed methodology for the detection of the wave systems is depicted in Figure 4.4: the wind-sea and primary and secondary swells partitions (i equals to 1, 2 and 3, respectively) are split over a matrix which comprises all the sea states classifying in the $H_s > 1m$ criterion, as shown in the top box. The next step of the procedure consists of assigning a colour from the black to white colour band (or pixel intensities between 0 and 255 respectively) to the occurrence of the gathered pairs (T_m, θ_m) from the matrix defined previously, as indicated in the middle panel of Figure 4.4. Thus, it is possible to apply Otsu's pixel group separation methodology, in which greater dissimilarity of pixel intensities is used, allowing to identify the systems and their respective centroids associated with the centroid matrices, i.e. the pairs (T_m, θ_m), as represented in the bottom panel of Figure 4.4.

In view of the above, the detection of the wave systems relies on frequency matrices whose number of pixels depends upon the bins widths, the choice of which therefore plays a pivotal role. These were calibrated at several nodes randomly selected among the hindcast series (Figure 4.1). Overall, the best performing set was found to be equal to 0.5 s and 5° for T_m and θ_m, respectively: indeed, a sensitivity analysis obtained by perturbing the bins width in the surroundings of such values (up to 1 s and 10°) yielded stable systems. By contrast, using very fine ranges (such as 0.1 s and 1°) would often lead to pictures populated by too many pixels, making hard to distinguish between the centroids of the resulting systems (i.e., they would lie very close to one another), while very wide intervals would group together wave systems with different characteristics and lead to a 'blurred' figure.
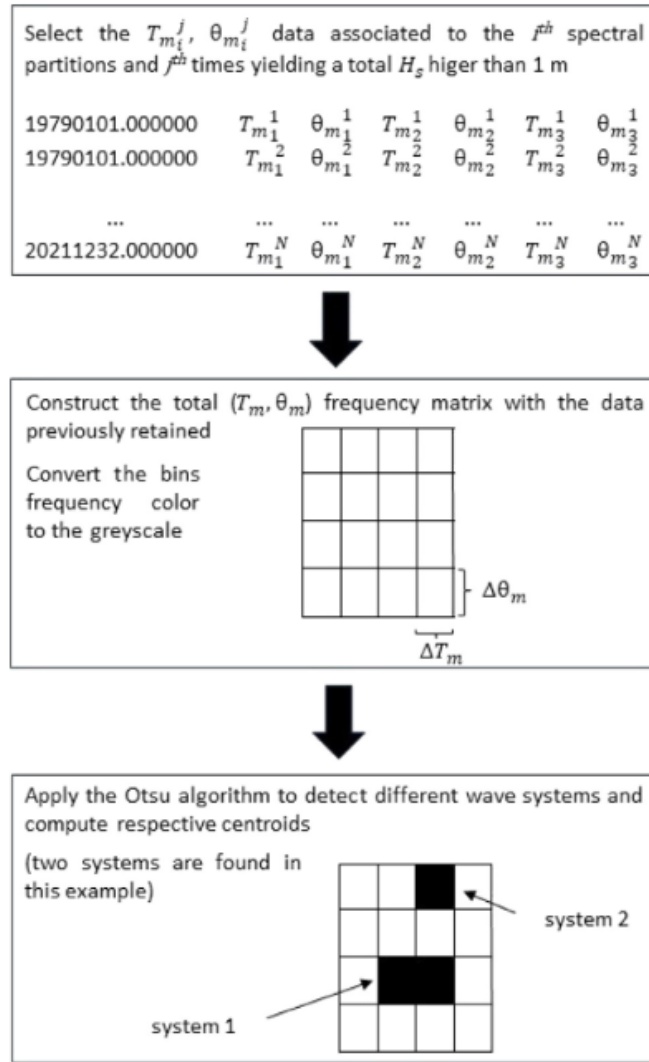
Figure 4.4: Workflow of the wave systems detection.

4.2.3. Crossing seas frequency of occurrence

The second step in this part of the study requires to group the data of each spectral partition according to the directional wave systems, based on the minimum Euclidean distance between their integral θ_m and those related to the systems centroids. It follows that for each hindcast time-step, beside the integral and peak parameters, the three spectral partitions are also associated to a flag indicating the wave system they belong to. This way, it becomes straightforward to assess the most frequent systems combination, or, in other words, where do crossing seas more likely come from:

$$f_{X,Y}(i,j) = \frac{n_{X=i,Y=j|H_{m0}\ X,Y\ >1m}}{N_y}, \tag{4.16}$$

where N_Y is the number of years of the time-series and $n_{X=i,Y=j}$ denote the number of

occurrences where the Xth and Y^{th} spectral partitions belong to the $_i$ and $_j$ systems, respectively. Note that, in this case, it is only retain the two most energetic partitions (X and Y) for each time step, provided that they yield a resulting wave height higher than 1 m. Since the total energy of the spectrum is the sum of the energies of the spectral partitions, it is easy to demonstrate that such condition reads:

$$H_{m0}^{XY} = \sqrt{H_{m0^X}^2 + H_{m0^Y}^2},$$
(4.17)

H_{m0^X} (H_{m0^Y}) being the spectral wave height of the Xth (Y^{th}) partition. Equation (4.16) can be then computed for all m pairs of wave systems, m being equal to:

$$m = n + \frac{n!}{2!\,(n-2)!},$$
(4.18)

where n corresponds to the total number of wave systems. From equation (4.18), it follows that also repeated systems are listed (for instance (1,1), (2,2), etc.), implying that the respective partitions will be likely characterized by directions of propagation close to one another. In fact, this may not be consistent with previous definitions of crossing sea, which require values of $\Delta\theta$ in between 45° and 135°, said $\Delta\theta$ the distance between two crossing waves direction (on the other hand, a following condition and an opposing condition are associated to $\Delta\theta > 45$ ° and $\Delta\theta < 135°$, respectively) [Donelan et al., 1997, Davison et al., 2022].

However, previous research found that, in case of multiple systems, higher waves are generated for $\Delta\theta$ lower than 40° [Onorato et al., 2010, Bitner-Gregersen and Toffoli, 2014, Zhang and Li, 2017], hence it is not initially exclude any possible permutation for computing the frequency of occurrence of oblique waves.

4.3. Results

4.3.1. Wave systems detection

Henceforth, for the sake of brevity reference is made to node 6858 (longitude 11.2900°, and latitude 38.8200 °) in the South Thyrrenian Sea, as show in Figure 4.1.

There, four systems are detected based on the workflow of Figure 4.4, as also clearly visible by the frequency matrix (Figure 4.6, right panel). The Otsu segmentation method allowed to reach this findings as shown in the segmented white and black image shown in Figure 4.5 (B).

According to the systems centroids (left panel 4.6), most waves propagate from $\approx 270°$ N (i.e., eastward according to the nautical convention; that is system 2), consistently to the extended W to E oriented fetch.

Nonetheless, given that the node is located in open waters, relevant systems can be appreciated with respect to multiple directions, i.e., N to S (system 1) and SE to NW (system 4), with even a reduced number of waves traveling SW (system 3). The systems weakly depend on the domain discretization: increasing the bins width to 10° (θ_m) and 1 s (T_m) yields negligible variations in the centroids coordinates, i.e., as high as 0.3 s and 2° at most for θ_m and $_m$, respectively.
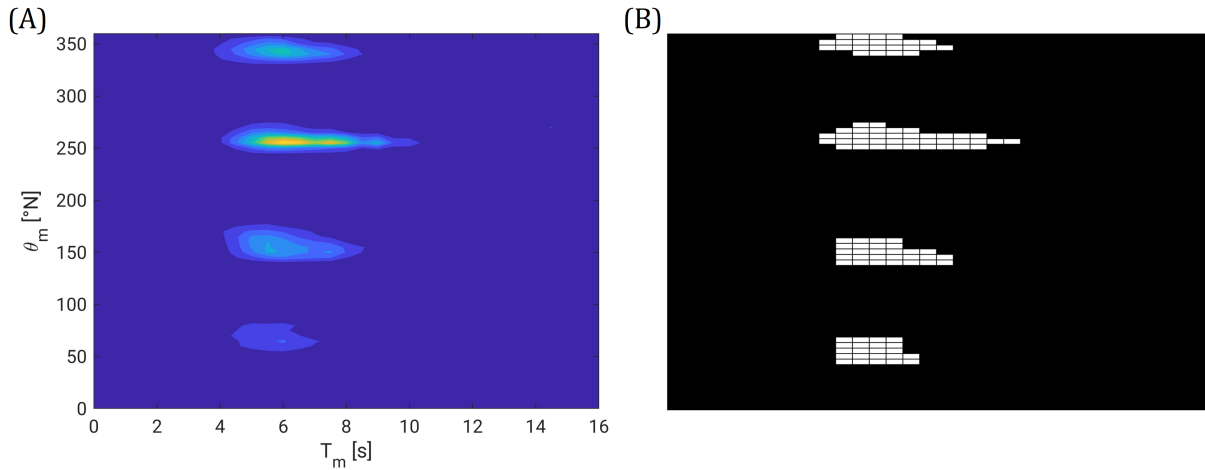
(A)

(B)

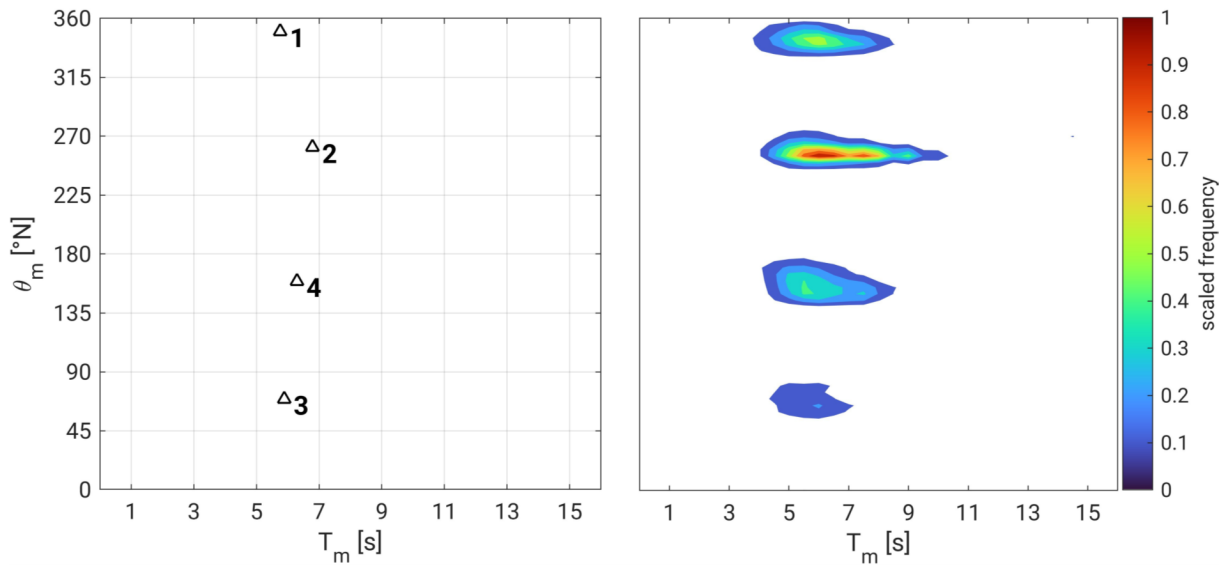Figure 4.5: Detection of the wave systems by means of Otsu's thresholding method.

Figure 4.6: Wave systems detected at node 6858. Left panel: centroids of the systems in the (T_m,θ_m) space; right panel: 2D-histogram of the (T_m,θ_m) distribution; colors represent the occurrence frequency scaled to the 0-1 space.

The four systems identified can be also appreciated in the polar diagrams, showing the T_m values relative to the respective wave angles for the first, second and third partition (panels A, B, and C of Figure 4.7, respectively). In fact, markers show separate point clouds well clustered around the centroids (indicated through their numbers; see the left panel of Figure 4.6), with few data lying in between systems. This consideration holds especially in case of the second and the third partition (panels B and C, respectively). The 1st partition, which refers to the wind seas, is indeed more densely populated, since the Mediterranean is a wind-dominated environment [Toomey et al., 2022].

Consequently, θ_m values are more scattered over the $0-2\pi$ space (Figure 4.7 A). However, no clear differences can be seen in the polar diagrams as regards θ_m since swell systems rarely
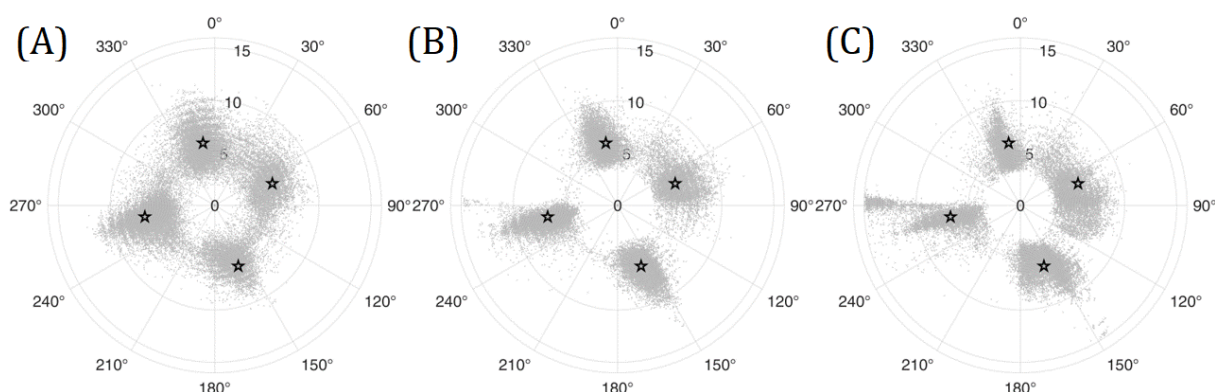
Figure 4.7: Polar plots of the integral parameters related to different spectral partitions at node 6858 (only dates with multiple partition available are retained). Panels (A), (B), and (C) denote the first, second, and third partition, respectively.

occur in the Mediterranean Sea and the spectral models may fail to distinguish the correct number of peaks. Besides, it is not possible to appreciate a prevailing contribution of any partition to none of the systems detected, as the former do not depend upon the waves direction; indeed, data span the whole 0–2π space for all cases (panels A, B, and C in Figure 4.7). Such drawbacks are overcome by remapping all available data according to the wave systems extracted.

Overall, the method proves to be efficient when wave systems are clearly separated between each other, allowing to identify up to 6 systems as in case of node 2695 (Figure 4.6 B). By contrast, when directional wave patterns lie very close in the θ_m space, they are hardly associated to independent systems, as shown for example in node 1102 for θ_m values lying in the third quadrant (Figure 4.6 A): in this case, the respective centroid does not efficiently capture the two bulks corresponding to approximately 225° and around 270°. Apart from this shortcoming, wave systems at node 1102 show that the methodology can handle the discontinuity between 0° N and 360° N in the directional domain, since waves propagating south are clustered together regardless of their θ_m (i.e., either they are close to 0° N or to 360° N, both directions indicating waves traveling south).

When extending the analysis to all hindcast nodes, the directions of the most frequent wave systems centroids reveal well known climatic patterns (Figure 4.8). In the Balearic Sea, the main traveling direction of waves is SW to NE (point B), mainly owing to the Vendavel winds [Lionello and Sanna, 2005], while along the Spanish coast wave mostly propagate from E/NE to W/SW (point C), as also pointed out by Sánchez-Arcilla et al. [2008], and Casas-Prat and Sierra [2010].

In the Gulf of Lion (point D), the wave climate is significantly affected by the prevailing Mistral winds (i.e., oriented from NW to SE [Obermann et al., 2018]), as well as in the Gulf of Sirte (point J) and in the Levantine Basin (point N), as highlighted e.g. by Zed et al. [2022]. This fetch seems to drive the whole climate in the South-Eastern Mediterranean Sea, with the exception of the waters south-west of the Crete Island (point M), which are mostly affected by southerly winds blowing over the Aegean Sea [Koletsis et al., 2009].

The Adriatic Sea is dominated by Sirocco waves (point K; direction of propagation from SE to NW) and Bora events in the upper part of the basin (point I; direction of propagation from NE to SW; [Benetazzo et al., 2022]), while in the Thyrrenian Sea (point H) and in the Gulf
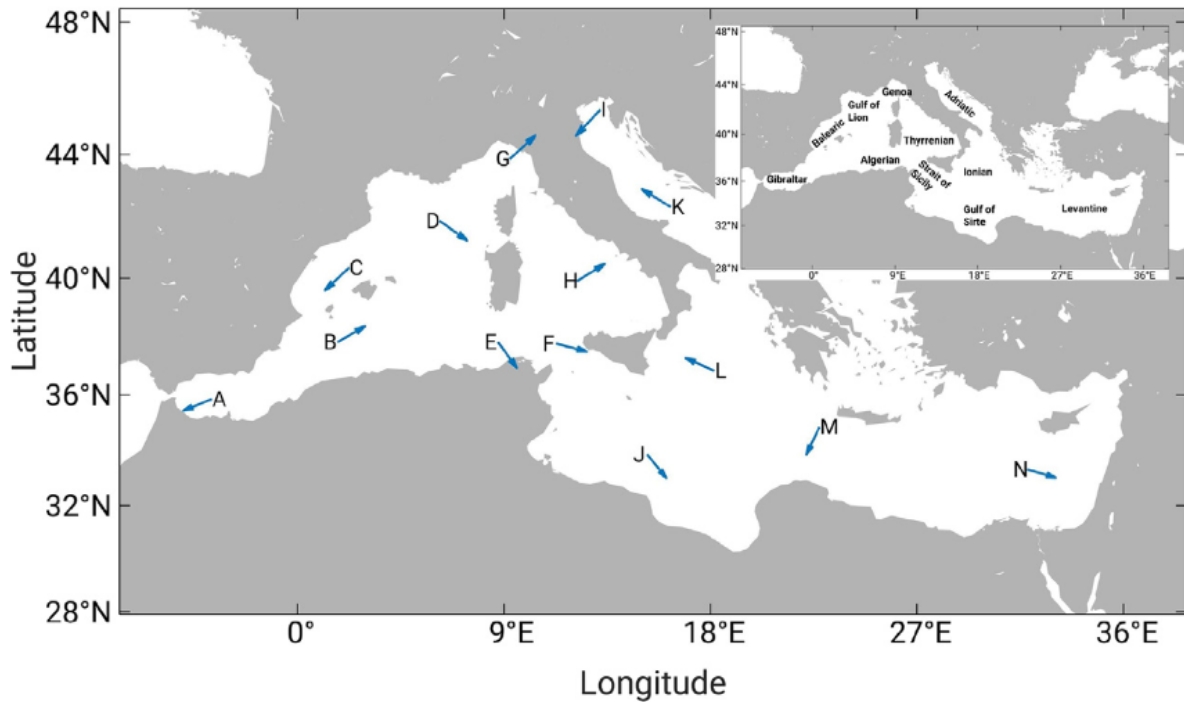
Figure 4.8: Directions associated to the centroids of the most frequent wave system. The inset reports the name of some sub-basins referenced in the text.

of Genoa (point G) the prevailing direction is Libeccio, that is SW to NE, as also shown by Saviano et al. [2020] and Cremonini et al. [2021], respectively.

Also in nodes F (Strait of Sicily), and L (Ionian Sea) the major directions are consistent to previous research in the area [Iuppa et al., 2015, Morucci et al., 2016, De Leo et al., 2020], although in the Ionian Sea there are sub-basins characterized by relevant southerly waves that would be overlooked if only retaining the most frequent wave system (see e.g. Federico et al. [2006]).

Similarly, in the Strait of Gibraltar (node A) there are two frequent systems associated to NW to SE and NE to SW directions, the latter being driven by the Levanter winds [Barbariol et al., 2021]; since the two systems are almost equally observed, they can be swapped at times between neighboring nodes, which may in turn exhibit diverging principal directions. Finally, along the Algerian coastline (point E), wave mainly propagate from N/NW to S/SE, as also pointed out e.g. by Amarouche et al. [2020].

The systems centroids also define the areas characterized by longer waves (Figure 4.7) such as the eastern Mediterranean Sea from the Algerian coastline up to the southern Gulf of Lion, which is indeed known to be affected by highly energetic sea states [Besio et al., 2016, Amarouche et al., 2020]; the Gulf of Sirte, where evidence of long period waves is present in the literature (Caloiero et al. [2022]); and the Levantine Sea. In the latter case, previous analysis highlighted higher mean wave climates clustered in between the Levantine and the Ionian Seas, hence characterized by a NW shift with respect to our findings (e.g. Zodiatis et al. [2014]).

However, it is stressed that the results presented here are tied to the mode of the (θ_m, T_m)

data at each site, hence they can greatly diverge from the mean wave climates depending on the basin considered, even more so when θ_m is concerned (compare in this respect results in Figure 4.8 to the mean wave directions in Elshinnawy and Antolínez [2023])

The wave periods associated to the most frequent wave systems do not seem to be related to the number of systems identified at the hindcast nodes. Our results reveal areas characterized by multiple systems in the Ionian Sea, the Gulf of Lion, the Thyrrenian Sea and the southeast Mediterranean Sea (Figure 4.8), which are indeed characterized by vast surfaces with multiple fetches available; conversely, bimodal wave climates are particularly clustered in the Adriatic Sea (i.e. Sirocco and Bora events) and in the Strait of Gibraltar which, being almost an enclosed basin, is only exposed to two relevant fetches, while three systems mainly characterize nodes lying closer to the coast with few exceptions (see for example the bunch of nodes off the Algerian coastline).

The majority of nodes lead to 4 and 5 systems (i.e. 362 and 241 out of 846, respectively), while only a few show either 2 or more than 5 systems (25 and 62, respectively, corresponding to $\approx 3\%$ and 7.3% of the total).

4.3.2. Assessment of crossing seas in the Mediterranean Sea

After assigning the data of each partition to the wave systems detected as explained in Section 2.3, it is possible to analyze the frequencies of the possible permutations at node 6858. Here, results show that (2,1) is the most frequent case (Table 4.1); indeed, these systems are associated to the highest rate of occurrence (see Figure 4.6). Such permutation indicates waves traveling E and S at the same time, as easily inferred by looking at the directions of the centroids involved, being equal to 261.5° and 350.0° (systems 2 and 1, respectively).

The directions of propagation related to the systems centroids are reflected on the $\Delta\theta_m$ distribution (Figure 4.9E), which is centered around 90°, indicating a crossing seas condition and proving that the centroids features are capable to summarize the characteristics of the majority of waves belonging to the respective systems.

Such consideration can be extended to the other permutations; for example, most of the $\Delta\theta_m$'s for the (2,4) permutation (Figure 4.9I) lie close to 100°, being the fourth system is associated to θ_m equal to 159.2°, while the (1,3) case yield a $\Delta\theta_m$ distribution spread around 75° (Figure 4.9F), with the third centroid's θ_m being approximately 69.2°N (i.e., difference between centroids direction equal to 79.2°). When different partitions belong the same system, the resulting $\Delta\theta_m$ distributions are shifted toward a following seas condition, as shown in panels (A), (B), (C), and (D) of Figure 4.9. This result is not surprising, as in these cases the directions of different partitions are closer to one another; however, it can be noticed how, in case of the (3,3) permutation, waves obliquity still denote more frequent crossing seas, owing to the broader dispersion of the waves directions belonging to the 3rd wave system (see in this respect the grey markers in Figure 4.7).

When the total H_{m0} exceeds 1 m, the most energetic partitions are mostly associated to crossing seas, as shown by the yearly rate of occurrences of the permutations considered, which result in around 23 and 22 days per year in case of permutations (2,4) and (2,1), respectively (Table 4.1), that are the most frequent cases in the node considered. By contrast, when refining
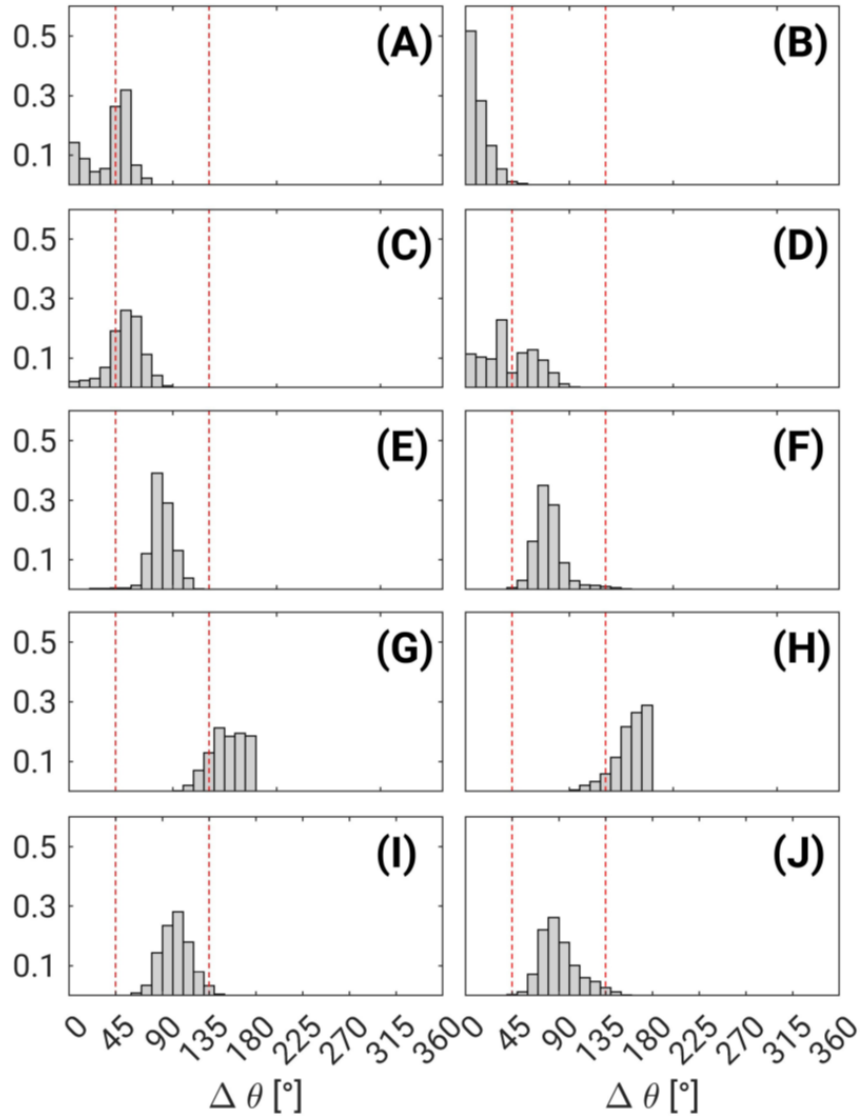
Figure 4.9: Frequency of waves obliquity according to different systems permutation. Panel (A): 1,1; panel (B): 2,2; panel (C): 3,3; panel (D): 4,4; panel (E): 1,2; panel (F): 1,3; panel (G): 1,4; panel (H): 2,3; panel (I): 2,4; panel (J): 3,4. Red dashed lines correspond to $\Delta\theta_m$ equal to 45° and 135°, i.e. the upper limits for following and crossing seas, respectively, according to Donelan et al. [1997].

the analysis as to account for the most critical cases, that is an obliquity in between 15° and 45° [Onorato et al., 2010, Bitner-Gregersen and Toffoli, 2014, Zhang and Li, 2017], the most frequent permutation is (2,2) (about 10 h per year), indicating waves traveling east (Table 4.2).

The frequency of partitions yielding H_{m0} greater than 1 m (regardless of their obliquity) is higher in the Eastern Mediterranean Sea, i.e., off the Gulf of Lion and in front of the Algerian coastlines, and in the south-west Ionian Sea (Figure 4.10A), with locations counting as many as approximately 110 days per year with such occurrences which, by contrast, are more seldom observed in the Adriatic Sea and the eastern Levantine Basin (approximately 50 days per year at most).

Table 4.1: Mean rate of occurrence [hours/year] of different systems permutations for partitions yielding $H_{m0} >1$ m.

S1 \ S2	1	2	3	4
1	2.2	526.6	185.0	83.9
2	- -	30.5	116.3	562.4
3	- -	- -	14.2	140.4
4	- -	- -	- -	7.1

Table 4.2: Mean rate of occurrence [hours/year] of different systems permutations for partitions yielding $H_{m0} >1$ m and $\Delta\theta_m$ in between $15°$ and $45°$

S1 \ S2	1	2	3	4
1	0.5	4.4	0.6	0.0
2	- -	9.9	0.0	0.1
3	- -	- -	2.5	0.3
4	- -	- -	- -	2.8

These patterns are not mirrored in the spatial distribution of partitions characterized by waves obliquity in $[15;45]°$ (say $f_{H_{m0}>1m|\Delta\theta_m \in [15;45]°}$; see Figure 4.10B): in this case, the highest frequencies of occurrence are found along the southern coasts of the Mediterranean Sea, with peaks located in the Nile's Delta area and the eastern part of the Strait of Gibraltar basin (up to approximately 14 days per year). These results can be linked to some extent to the number of wave systems detected at the hindcast nodes (Figure 4.8), which, on average, show multi-modal wave climates in open waters, where partitions belonging to different systems occur more frequently.

On the other hand, spectral partitions do more easily belong to the same system when only a few are available, therefore resulting in wave directions almost aligned and, in turn, higher occurrences associated to lower waves obliquity; however, the correlation between the number of systems and $f_{H_{m0}>1m|\Delta\theta_m \in [15;45]°}$ across all hindcast nodes is only equal to 0.4, thus other features, to be investigated on a single basis case, may play important roles as well.

In general, the permutations not only provide an insight into the joint occurrence of such combinations of wave systems, but also reveal periods associated with wave conditions in which the occurrence of certain types of partitions or governing characteristics in a specific location are unfavourable for the development of activities with an anthropogenic component. For example, depending on the permutations determined for a locality, the placement of an attenuator or terminator wave energy converter could be defined which depends strongly in the dominant wave direction, and the period of shutdown of operation of such converters. The wave system permutations analysis previous to a time and spatial planning provides a safety to the maritime routes of vessels.

Moreover, through permutations such as the one shown for example of the permutation (2,2) in Table 4.1, not necessarily for the crossing seas of the permutation with the highest occurrence the most extreme conditions ($f_{H_{m0}>1m|\Delta\theta_m \in [15;45]°}$) are reached (Table 4.2); suggesting that the
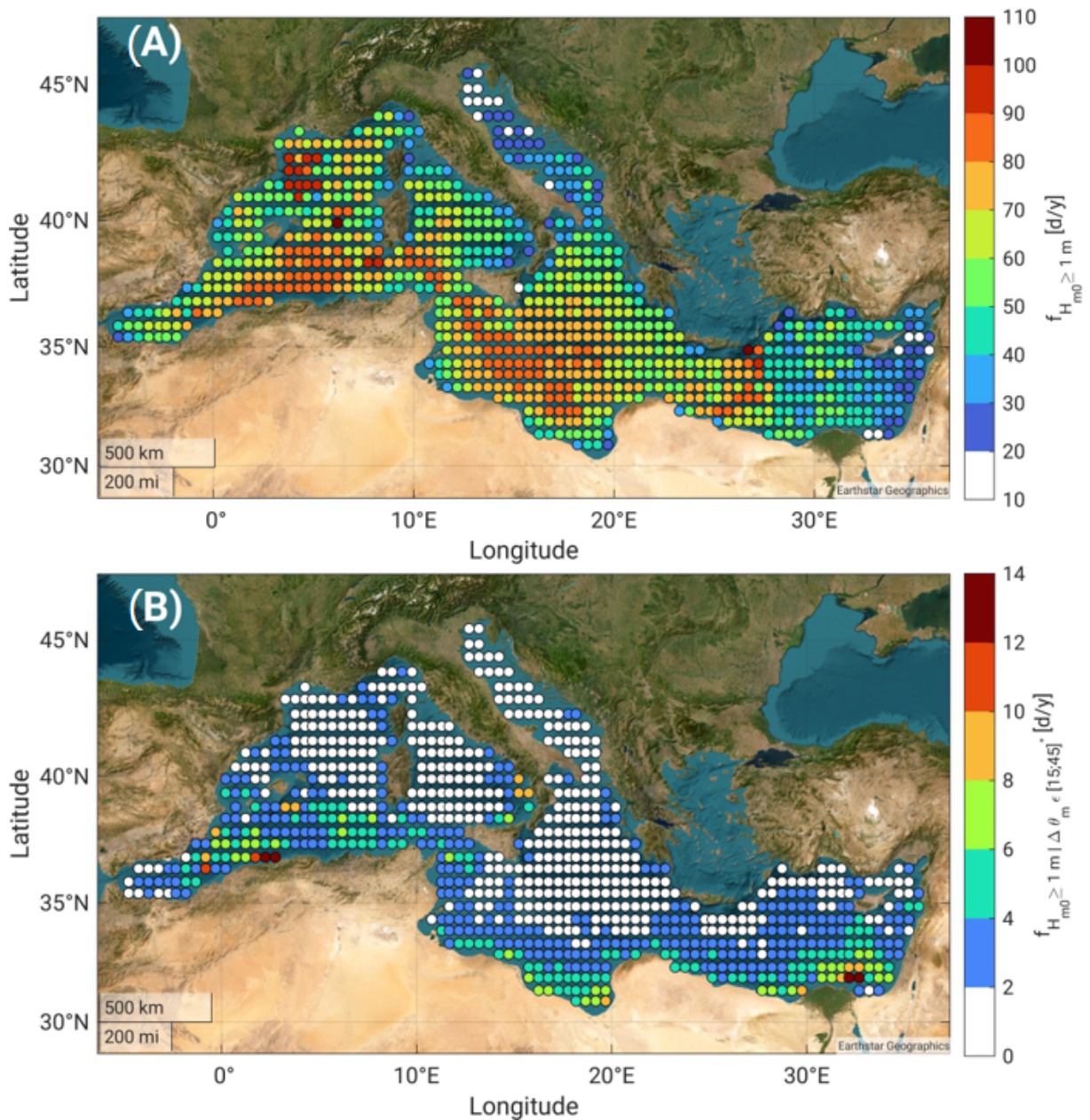
Figure 4.10: Maps of wave system frequencies (days per year): chart (A) shows the frequency for all wave systems, whereas chart (B) related to the crossing seas.

further assessment of wave systems identification and their combination, i.e. estimation of the permutations, is required to describe the potential risk more appropriately.

Finally, the free availability of information on the permutation of wave systems and their occurrence is highlighted; it can be found on the website indicated in the following link: http://www3.dicca.unige.it/meteocean/wave_systems/html/systems_map.html. A snapshot of this webGIS is shown in Figure 4.11.
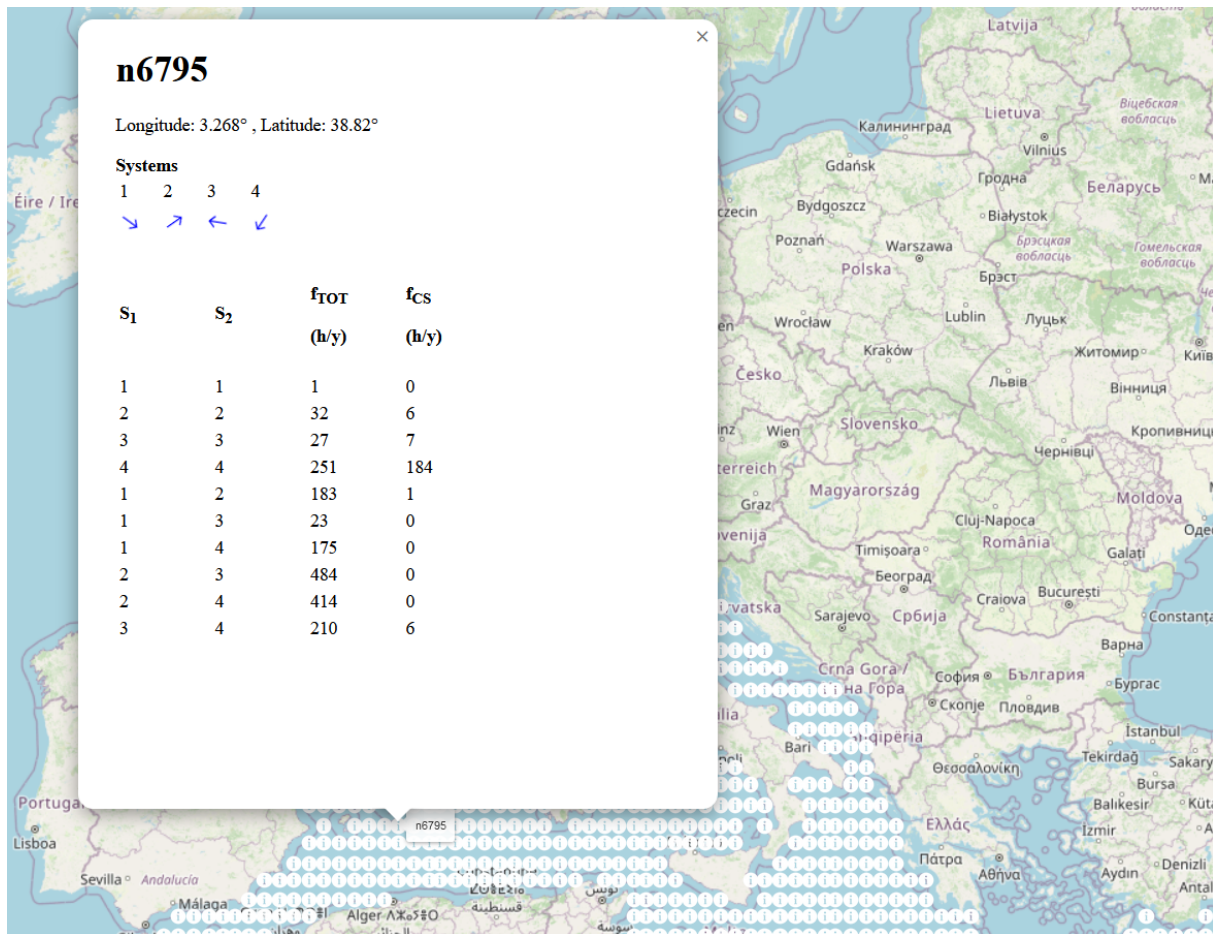
Figure 4.11: Snapshot of the frequency of occurrence of the wave systems in one specific location in the Mediterranean Sea.

4.4. Final remarks

The present wave systems analysis along the Mediterranean Sea as introduced an innovative approach for identifying significant directional wave systems at a specified location. By integrating an image processing algorithm, based on the combination of the spectral parameters T_m and θ_m, wave climate modes linked to specific propagation directions can be accurately extracted. This method effectively addresses the limitations of conventional spectral partitioning methods, which often overlook essential directional features necessary for various applications.

The analysis has demonstrated the robustness of the methodology, especially in regions experiencing multimodal wave climates originating from various fetches. The wave systems extracted have provided valuable insights into the frequency of complex wave occurrences, such as crossing seas characterized by simultaneous waves from different directions. By leveraging this methodology, the most frequent directional wave systems in the Mediterranean Sea have been successfully identified, using hindcast data spanning the entire basin. The results are in line with well-established climate patterns observed in previous studies, suggesting potential

extensions of similar analyses to other seas and oceans globally.

Moreover, the identified directional wave systems have been used to evaluate the frequency of potentially hazardous sea states for navigation, focusing on waves with obliquities ranging from 15° N to 45° N [Bitner-Gregersen and Toffoli, 2014]. Indeed, the highest occurrences of crossing seas were detected as shown in the Figure 4.10: in Nile's Delta area, wherein the occurrences arrive up to 14 days per year; a similar situation occurs in the eastern part of the Strait of Gibraltar basin with crossing seas ocurrence between 6 to 14 days per year, approximately. Crossing seas occur with less intensity in the Gulf of Sidra in Libya, where the occurrence can vary between 6 to 10 days per year.

This wave direction range (15° N to 45° N) was chosen based on analytical studies of crossing seas and historical data on wave conditions during maritime accidents [Zhang and Li, 2017]. Notwithstanding, it is essential to note that the response of different vessels to varying wave conditions, as well as the influence of traffic routes and operating conditions, can significantly impact accident occurrences, as emphasized in prior research.

Despite these complexities, the use of limited information, primarily related to spectral partitions, has enabled a comprehensive understanding of the wave climatology of the Mediterranean Sea. This lays the groundwork for future applications in offshore and coastal engineering design, catering to navigation safety and coastal protection requirements.